Original Article

Multifunctional and durable graphene-based composite sponge doped with antimonene nanosheets

Check for updates

Yin Yu [a], Qingshi Meng [a,b,**], Tianqing Liu [c,*]

[a] College of Aerospace Engineering, Shenyang Aerospace University, Shenyang, 110136, China
[b] Shenyang Aircraft Design Institute, Shenyang, 110035, China
[c] NICM Health Research Institute, Western Sydney University, Westmead, 2145, Australia

ARTICLE INFO

ABSTRACT

The development of flexible multifunctional composites is an important topic in the fields of materials engineering, electronics, aerospace and biomedicine. However, there are still major challenges to achieve a variety of functions to meet the requirement for the application. Herein, a flexible multifunctional porous composite is successfully prepared by fabricating both modified graphene and antimonene into a melamine sponge. Compared with the graphene composite sponge, the addition of antimonene improved its electrochemical and sensing performances. The specific capacitance of antimonene/graphene composite sponge was significantly increased, while the capacitance retention rate was 83% under 20,000 charge—discharge cycles. The pressure sensitivity of the prepared flexible multifunctional device assembled was 44% higher than that of the graphene composite sponge. A power supply-integrated sensing system was assembled for monitoring human motion signals. The experimental results show that this system is a promising monitoring device with broad potentials in the fields of biosensing.

© 2022 The Author(s). Published by Elsevier B.V. This is an open access article under the CC BY-NC-ND license (http://creativecommons.org/licenses/by-nc-nd/4.0/).

1. Introduction

Porous functional composites have significant advantages, including ultra-high surface area, light weight, desirable compressible performance, tensile elongation and good energy absorption, compared with conventional film materials [1—3]. Although porous functional materials have been widely researched, their further development in the industrial field is affected by the fact that they are normally prepared with a single function and cannot meet diverse industrial requirements for applications, such as solar-driven clean water generation, electrochemical sensors and heaters [4—7]. Therefore, the development of multifunctional applications of porous composites has become a research hotspot in the fields of aerospace, biomedicine, and electrochemistry [8—10]. Multifunctional porous composites can be engineered to simultaneously meet the mechanical, thermal, acoustic and

energy absorption requirements through the design of the internal structure of the multifunctional porous composite [11—14]. The multifunctional porous composites are prepared by various methods, vacuum impregnation method, electro-spinning, in-situ polymerization and template method [15—17], among which the most common method is to combine the functional fillers with the porous matrix [18—21].

Fillers are the key factor affecting the performances of multifunctional porous composites. Two-dimensional nano-sheets are widely used as functional fillers because of their unique structure with large specific surface area and prominent properties. Graphene has been extensively investigated as one of the most promising two-dimensional filler for creating multifunctional composites due to their excellent electrical conductivity [22,23], high mechanical strength [24,25], thermal conductivity [26,27] and regular two-dimensional structure [28]. For example, Chen et al. [29] produced a low packing graphene micropopcorn (GMP) with a hollow structure as a highly effective conductive filler for multifunctional composites. This micro form of graphene greatly improved the thermal conductivity and microwave absorption performance of the composites. Qiu et al. [30] modified multilayer graphene with poly (2-aminothiazole) to produce a multifunctional composite coating with good corrosion resistance and wear reduction performance. Although graphene has excellent properties in thermal, electrical and other functional areas, its applications in the electronic and optoelectronic fields are limited by the bandgap requirements [31,32].

Antimonene is a new two-dimensional semiconductor material with excellent optoelectronics and spintronics properties [33—36]. It is a graphene-like structure with wrinkles composed entirely of Sb atoms [37]. Monolayer and few-layer antimonene have indirect band gap and high electron transfer rate [38]. Their indirect band gap characteristics can overcome the limitations of graphene as a semiconductor device, making them excellent candidates for microelectronic applications [39—41]. At present, it has been reported that chemically stable few-layer antimonene can be prepared by mechanical exfoliation [42], liquid phase exfoliation [43], epitaxial growth [44] and other methods [45]. However, most of the reported methods have disadvantages, such as time-consuming preparation, strict solvent ratios and high oxidation tendency. An efficient, stable and simple exfoliation method remains to be explored. Therefore, in this paper, an aqueous solution of surfactant is used as the exfoliation environment of antimonene. On the one hand, the surfactant improves the dispersion of antimonene in aqueous solution, which makes it possible to exfoliate antimonene in aqueous solution. On the other hand, the surfactant protects antimonene from air and water oxidation, and a stable antimonene solution can be prepared in a short preparation time.

Recent reports indicate that antimonene has excellent performance in Li^+/Na^+ ion batteries, electrocatalysis and other applications [46—48]. Because the high specific surface area of the layered structure promotes more electrode—electrolyte interactions at the interface, the specific capacitance values of composites prepared by antimonene are relatively high [49]. When antimonene is used as a functional filler to compound

with other matrix materials, the free movement of charge carriers can be ensured when it is distributed on the surface or inside the matrix, leading to better electrochemical performance of the whole material. In addition, the nanostructure of antimonene makes it easier to transfer electrons to the collector, which can significantly increase the efficiency of electron collection. The fast reversible ion adsorption and desorption kinetics of antimonene greatly improved the power and energy density, long cycle stability, mechanical stability and structural stability of the materials [50]. However, there are few experiments on adding antimonene to graphene composites to improve their electrochemical performance, sensitivity and stability for applications in supercapacitors and sensors [51—53].

In this paper, we used aqueous dispersion of an organic solvent to provide a stable environment for exfoliating antimonene and ensure structural regularity of graphene sheets by the physical modification. Modified graphene sheets and antimonene were uniformly attached to the sponge skeleton based on a solution blending method, while the melamine sponge was used as flexible substrate to prepare the antimonene/graphene composite sponges. The prepared antimonene/graphene composite sponges were applied as supercapacitor and capacitive sensors. In the preparation process of capacitive sensors, conductive carbon cloth and solid electrolyte were introduced to assemble flexible wearable sensors. In this work, the micro-morphology of the antimoene/graphene composite sponges, the electrochemical properties and sensing performance of the functional devices were characterized. The influence of antimonene doping concentrations on the electrochemical performance of composite materials was studied. Their application and practical prospect in monitoring human knee, elbow and wrist bends was explored. The results showed that the use of antimonene greatly improved the electrochemical properties and the sensitivity of graphene sponge materials used as multifunctional sensing devices, while maintaining the electrical conductivity of materials. The sensing system can also effectively monitor human motion signals, suggesting their great potentials in biomedical and electronic sensing applications.

2. Experimental section

2.1. Materials

Graphite intercalation compound (GIC, 1395) was kindly supplied by Asbury Carbons (Asbury, USA). Antimony (Sb, purity $\geq 99.99\%$, granularity 5—50 mm) was kindly supplied by Guantai Metal Materials Co., Ltd. (Beijing, China). The commercial sponge (tripolycyanamide) with the density of 15—17 kg/m^3 was provided by Xijie Co. Ltd. (Hubei, China). The porosity was 88.725% ± 0.53%. Triton®X-100 was purchased from BioFroxx (Bruckberg, Germany). ED-2003 (polyether amines with diamines) was provided by Liansheng Trading Co. Ltd. (Dalian, China). Conductive carbon cloth was provided by Shanghai Hesen Electronics Co. Ltd. (Shanghai, China). Polyurethane (PU) film was purchased from Ruicao Pharmaceutical Equipment Packaging Hall (Hebei, China). Potassium hydroxide (KOH) and polyvinyl alcohol (PVA) were supplied by
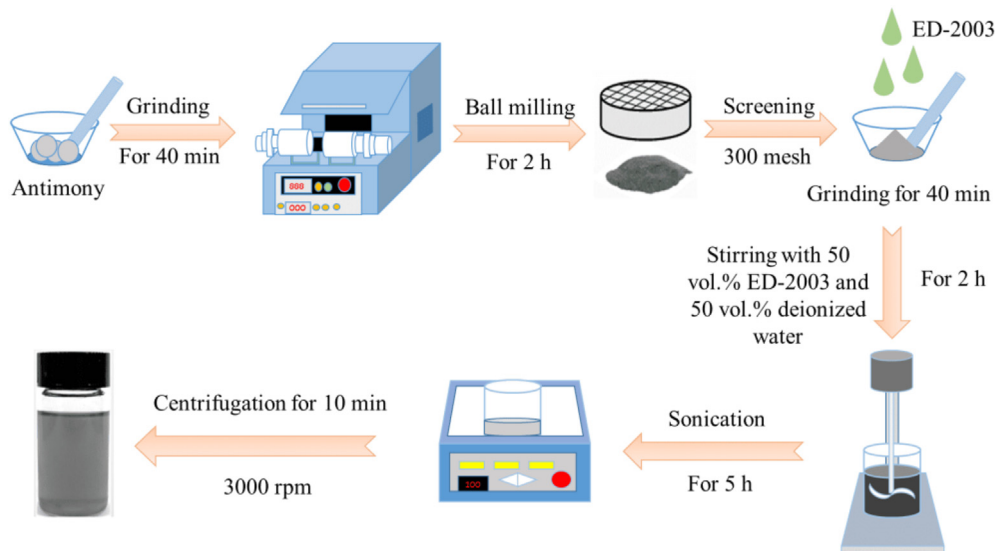
Fig. 1 — The schematic diagram of preparation process of the few-layer antimonene solution.

Tianjin Science and Trade Co. Ltd. (Tianjin, China). All materials were supplied without further purification.

2.2. Device fabrication

2.2.1. Preparation of the few-layer antimonene solution
The schematic diagram of preparation process of the few-layer antimonene solution is shown in Fig. 1. Antimony particles were pretreated by grinding for 40 min in a ceramic mortar. After grinding into uniform powder, it was stirred in a ball milling reactor for 2 h at 800 rpm with the ratio of grinding media (stainless-steel balls) to material = 5:1. The resulting antimony particles were separated from the stainless-steel balls by washing with alcohol. The dried powder was then screened with a 300-mesh sieve. The material was ground for 40 min in the ratio of 1 ml ED-2003 per 1 g antimony powder. Deionized water (10 ml) and ED-2003 solution (10 ml) were added and stirred mechanically for 2 h. After ultrasonic treatment for 5 h and centrifugation at 3000 rpm for 10 min, the supernatant was collected and modified few-layer antimonene solution was obtained.

2.2.2. Fabrication of graphene sheets
The preparation method of graphene sheets was described according to our reported method [54,55]. As shown in Fig. 2, a crucible containing the graphite intercalated compound was placed in a muffle furnace heated to 700 °C for 3—4 min. After

cooling, the expanded graphene sheets were put into acetone solution and treated with ultrasonication at 25 °C for 3—4 h. Finally, they were dried in an oven with 80 °C to get the final graphene sheets.

2.2.3. Fabrication of antimonene/graphene composite sponge
The fabrication process of antimonene/graphene composite sponges is illustrated in Fig. 3. Graphene sheets (0.06 g) was placed in an agate mortar and 0.3 ml of Triton was added to grind the mixture for 40 min. The modified graphene sheets were added to 120 ml of deionized water during stirring for 2 h. The prepared few-layer antimonene solution was evenly mixed with graphene sheets solution and then treated by ultrasound for 1 h. The sponge was placed into the mixture with ultrasonic treatment for 10 h and then dried at 80 °C. The antimonene/graphene composite sponges were optimized by mixing with different weight ratios of the graphene sheets and antimony and different ratio of surfactant and fillers (Table 1) (see Fig. 4).

2.2.4. Assembly of functional device
To prepare the PVA/KOH gel electrolyte, PVA (3 g) and KOH (3 g) were added in 30 mL of distilled water and stirred at 90 °C until the solution became clear. The PVA/KOH gel was applied in between two antimonene/graphene composite sponge electrodes to act as both electrolyte and separator. The whole device was then dried in an oven at 50 °C. The carbon cloth
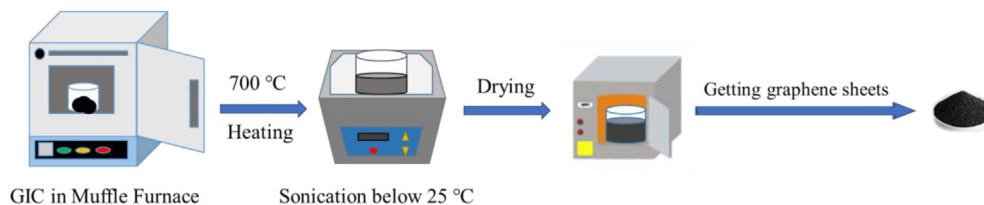
Fig. 2 — The schematic diagram of preparation process of graphene sheets.
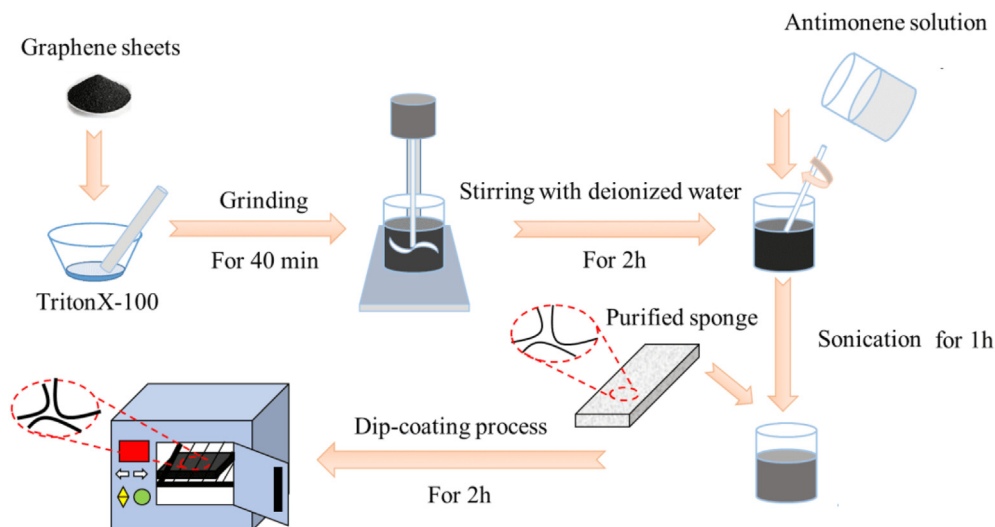
Fig. 3 — The diagram of the fabrication of the antimonene/graphene composite sponge.

was cut into two rectangles with a size of 10 × 2 cm and placed on both sides of the device. Finally, we encapsulated the whole device with PU films.

2.3. Characterization

The thickness of graphene sheets and antimonene nanosheets were analyzed by an atomic force microscope (AFM, Dimension ICON2-SYS, Brook company, USA). The surface structure of antimony particle and the interior structure of antimonene/graphene composite sponges with different ratios of surfactant and fillers were observed by a scanning electron microscope (SEM, SU8010, Hitachi, Japan) with an accelerating voltage of 5 kv.

Tensile strength and elongation of the antimonene/graphene composite sponges with different contents were evaluated using universal tensile machine (GX-SF001, Shenzhen Shared instrument equipment co. LTD, China) with the strain rate of 2 mm/min at room temperature (RT = 25 °C). The overall

sample size was 6.00 × 2.00 × 0.25 ± 0.02 cm with gauge length of 35 mm.

An electrochemical workstation (CHI660E B19038, Chenhua Instrument CO., Shanghai, China) was used to analyze the electrical, capacitive and sensing properties of the antimonene/graphene composite sponges.

For two-electrode supercapacitor devices, the specific capacitance (C) is calculated from the area in the cyclic voltammetry (CV) curve [56—58]:

$$C = \frac{\int I \, dv}{v \triangle VM} \tag{1}$$

the energy density (E) and power density (P) are calculated by:

$$E = \frac{1}{2}C(\triangle V)^2 \tag{2}$$

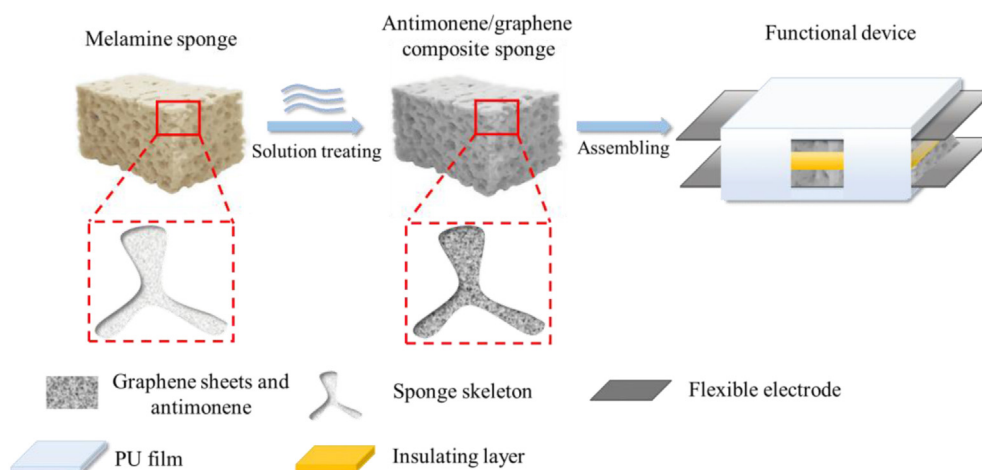$$P = \frac{3600E}{\triangle t} \tag{3}$$

Fig. 4 — The diagram of the assembly of the functional device.

Table 1 — The weight ratio between graphene sheets and antimony and the ratio between surfactant and fillers used in this study.

Sample	Weight ratio between graphene sheets and antimony	Ratio between surfactant and fillers
AG-1	1:0	Graphene sheets: Triton = 0.06 g: 0.3 ml
AG-2	1:1	Graphene sheets: Triton = 0.06 g: 0.3 ml Antimony: ED-2003 = 0.06 g: 0.06 ml
AG-3	1:1.5	Graphene sheets: Triton = 0.06 g: 0.3 ml Antimony: ED-2003 = 0.09 g: 0.09 ml
AG-4	1:2	Graphene sheets: Triton = 0.06 g: 0.3 ml Antimony: ED-2003 = 0.12 g: 0.12 ml
AG-5	0:2	Antimony: ED-2003 = 0.12 g: 0.12 ml

Where I is the current (A), v is the scan rate (V·s^{-1}), V is the working potential, M is the weight of fillers in the composite (g), and Δt is the discharging time.

3. Results and discussion

3.1. Morphology of the antimonene/graphene composite sponges

The distributions of antimonene and graphene sheets in the sponges were observed by the morphological analysis of the pure sponge and the prepared antimonene/graphene composite sponges with different contents (AG-1, AG-3 and AG-4). Figure 5 (a1-a3) showed that the pure sponge had a three-dimensional interconnection network with smooth skeleton structure and uniform pore distribution. The sponge electrodes had many pores accessible to electrolyte, providing abundant interfacial area for energy storage [59—61]. This suggested that it is possible for the antimonene/graphene composite sponges to be used as supercapacitor in the later studies.

The internal morphologies of AG-1 sample showed that the graphene sheets were randomly dispersed across the surface of the pure sponge in Fig. 5 (b1-b3). As shown in Fig. S1 of the Supporting Information, graphene sheets had large sizes with an average thickness of about 3.28 nm after thermal expansion-ultrasonication treatment. Such large surface area provided support for better attachment to sponge skeleton and bearing antimonene in the later stage. The enlarged image of Fig. 5b3 showed the folded structure of the graphene sheets stacked against each other, which made the distribution of graphene sheets on the sponge skeleton more obvious. Figure 5 (c1-c3) show the morphologies of AG-3 sample. The mixture of graphene sheets and antimonene uniformly adhered on the surface of the sponge skeleton from the micrograph is shown in Fig. 5 (c1-c2), reflecting the reliability of the preparation process. In Fig. 5c3, few-layer antimonene, as the nearly circular, granular bright spot highlighted by the red arrows, were evenly distributed on the surface of graphene sheets. Antimonene were prepared in an organic solvent medium by ultrasonication method. They showed uniform morphology and thin thickness in Figs. S2 and S3 of the Supporting Information. The position distribution of antimonene and graphene sheets illustrated that graphene sheets behaved like the carriers for antimonene, possibly due to the larger surface area of the graphene. Fig. S4 in Supporting Information also demonstrated the larger surface area of graphene sheets by comparing their suspension time antimonene with smaller surface area.

Moreover, there are many obvious aggregates formed in the composite material AG-4 with higher concentration of antimonene and organic solvent (ED-2003) compared with AG-3 in Fig. 5 (d1-d3). The existence of aggregates affects the uniformity of the internal structure of the composites, which will further affect their electrical conductivity, mechanical and functional properties. In addition, in the antimonene composite sponge without graphene sheets (AG-5 samples), granular antimonene cannot be uniformly covered on the sponge skeleton surface due to their small specific surface area (Fig. S5, Supporting Information).

The overlay, Sb and C elemental maps of AG-3 and AG-4 samples further confirmed the distribution of antimonene and graphene sheets on the sponge surface (Fig. 5 e1-f3). The green channel images showed the presence of Sb element in the sponges (Fig. 5e2 and f2), while the pink channel images showed the presence of C element (Fig. 5e3 and f3). The distribution of antimonene and graphene sheets was relatively uniform both on the sponge bone of AG-3 sample and in the aggregates of AG-4 sample, indicating the reliability of the preparation method. In order to explain the content of component elements, we carried out SEM element composition analysis. The contents of antimonene in AG-3 and AG-4 samples is 20.21% and 25.63%, respectively. Although the mass of antimony added in the preparation process is more than that of graphene sheets, the content of graphene sheets in the final prepared composite material is dominant (in Fig. S6).

3.2. Mechanical property of antimonene/graphene composite sponge

The tensile strength and elongation of antimonene/graphene composite sponges with different contents were compared with that of pure sponge. The tensile strength and elongation of the pristine sponge was 81.4 kPa and 21.77%, respectively (Fig. 6). The tensile strength of the composite sponge with the addition of graphene sheets increased to 159.4 kPa, while the elongation at break decreased slightly, suggesting the graphene with high mechanical properties attached to the sponge skeleton. With the addition of antimonene, the tensile strength of the graphene/antimonene composite sponges increased slightly from 137.8 to 141.7 kPa as the antimony contents varied from 0.06 to 0.12 g. The contents of antimonene in the composite materials are too small to influence on the mechanical properties of the whole composite materials. However, compared with the graphene composite
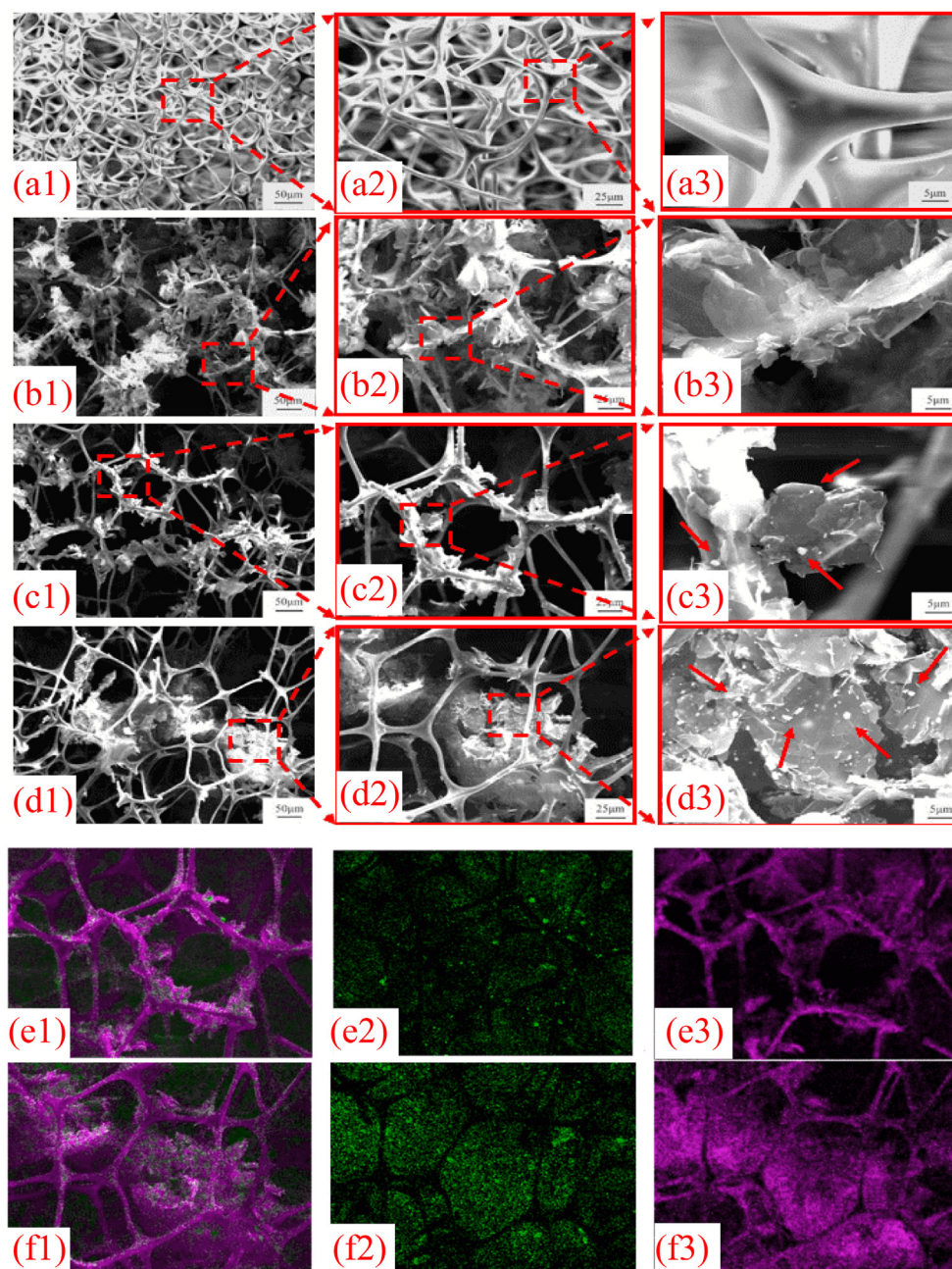
Fig. 5 − SEM images of the original commercial sponge (a1-a3), AG-1 (b1-b3), AG-3 (c1-c3) and AG-4 (d1-d3) samples; and the overlays and elemental maps of Sb and C in AG-3 (e1-e3) and AG-4 (f1-f3) samples.
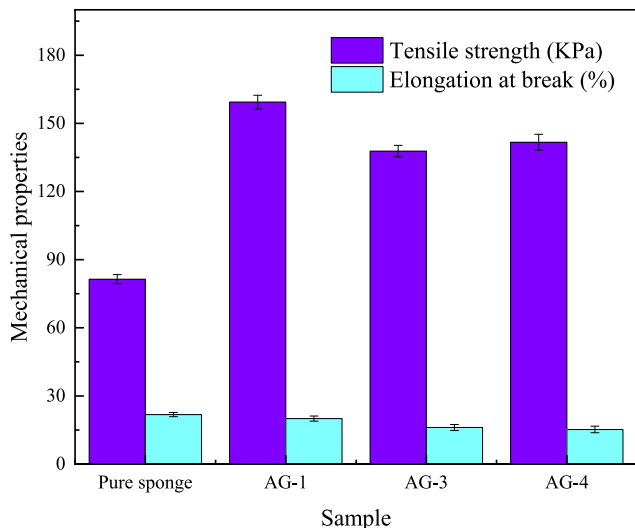
sponge, the tensile strength and elongation at break of the antimonene/graphene composite sponge decreased significantly. The phenomena may be due to the solidification of ED-2003 at RT during the preparation process, resulting in an increase in the hardness of the material.

A series of stress−strain tests were employed to characterize the mechanical property and self-recovery property of the antimonene/graphene composite sponges. The typical stress−strain curves demonstrated that as the increase in graphene sheets and antimonene contents, the strain ranges of the composite materials become narrower (Fig. S7a). This indicated that their addition increased the overall hardness of the composite materials. Since the dispersion of graphene and

antimonene in AG-3 sample is more uniform than that in AG-4 sample and acceptable mechanical properties, we selected AG-3 as the representative sample for the loading-unloading test. As presented in Fig. S7b in the Supporting Information, the consecutive loading−reloading curve is partially overlapped, indicating that the sample underwent the partial self-recovery process.

3.3. Temperature adaptability of antimonene/graphene composite sponge

Due to the uniform internal structure and acceptable mechanical properties of AG-3 samples, they were selected for

JOURNAL OF MATERIALS RESEARCH AND TECHNOLOGY 2022;17:2466—2479

Fig. 6 — Mechanical properties of the antimonene/graphene composite sponges with different filler contents by measuring tensile strength and elongation at break.

temperature adaptability study compared with AG-1 samples to investigate the effect of antimonene addition on the environmental stability of the composites. The results in Fig. 7a show that AG-1 and AG-3 samples are compressed to about half of their own height at 3.08 kPa (500 g weight) without permanent deformation, suggesting that they have good compression properties. However, the compressible thicknesses of AG-3 samples are significantly lower than those of AG-1 samples, possibly due to the increase in the overall hardness of the composite materials caused by ED-2003 curing in AG-3 sample preparation, leading to the decrease of compression performance. Nevertheless, AG-3 samples maintained good torsion and bending ability even when stored at −20 or 100 °C for 24 h (Fig. S8 in the Supporting Information).

The mechanical properties of the AG-1 and AG-3 samples at −20 °C and 100 °C, measured by tensile strength and elongation at break, kept almost unchanged compared with the ones at room temperature (Fig. 7b). It is mainly attributed to the high thermal stability of the graphene/antimonene-coated sponge skeleton, leading to the excellent temperature adaptability of antimonene/graphene composite sponge. However,

the performance of the AG-3 samples varies within a narrower range with temperature compared to AG-1 samples. These results also prove that the excellent adaptation property of the antimonene/graphene composite sponges had endowed good availability in the temperature range from −20 to 100 °C.

3.4. Electrical property of antimonene/graphene composite sponge

Figure 8a illustrates the current—voltage (I—V) curve of the antimonene/graphene composite sponges at different filler ratios, showing typical ohmic behavior. With the content of antimony increasing, the conductivity decreased accordingly. This is because the structured conductive network of graphene was affected by the addition of antimony. Additionally, the electrical conductivity of AG-3 increased with the increase of temperature from RT to 100 °C (Fig. 8b) This is associated with the presence of antimonene and graphene sheets in the sponge matrix, which made the whole composites exhibit semiconductor property. The excellent conductivity and thermomechanical stability expanded the potential application of the antimonene/graphene composite sponge in the fields of flexible sensing electronics.

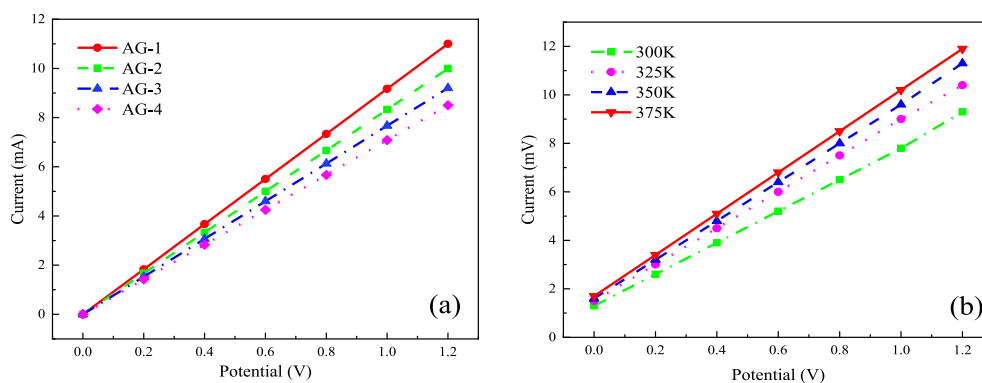### 3.5. Electrochemical performance of the functional devices

The prepared functional devices with various antimonene/graphene composite sponge contents (AG-1, AG-2, AG-3 and AG-4) were firstly applied as supercapacitors. Their electrochemical properties were examined in the dual-electrode configuration. The electrochemical characteristic of the functional devices was assessed by measuring cyclic voltammetry (CV) and constant current charge—discharge (GCD) in a dual-electrode system.

In Fig. 9a, the CV profiles of the functional devices with AG-1, AG-2, AG-3 and AG-4 samples are recorded over the potential window ranging from −0.6 to 0.6 V at a scan rate of 100 mV/s. Based on the area of the CV profiles, the contribution of capacitive performance of pure graphene composite sponge to functional device is almost negligible. In contrast, the current density observed in the CV profiles of the functional devices with antimonene/graphene composite sponge electrodes were enhanced compared with devices made from
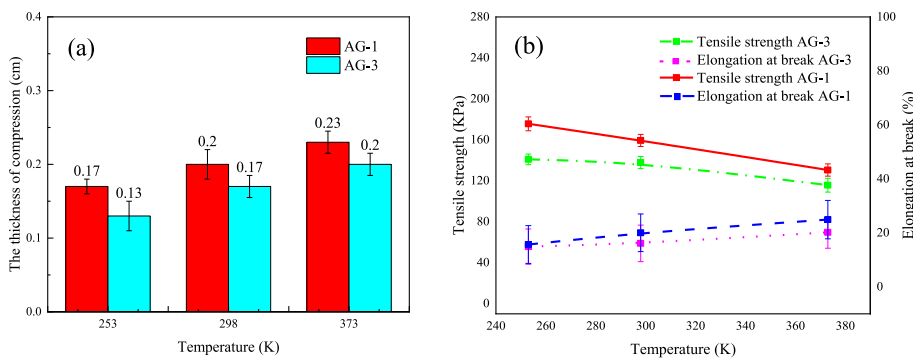
Fig. 7 — (a) The thickness of compression and (b) tensile strength and elongation at break at different temperatures (−20, 25 and 100 °C) for AG-1 and AG-3 samples.
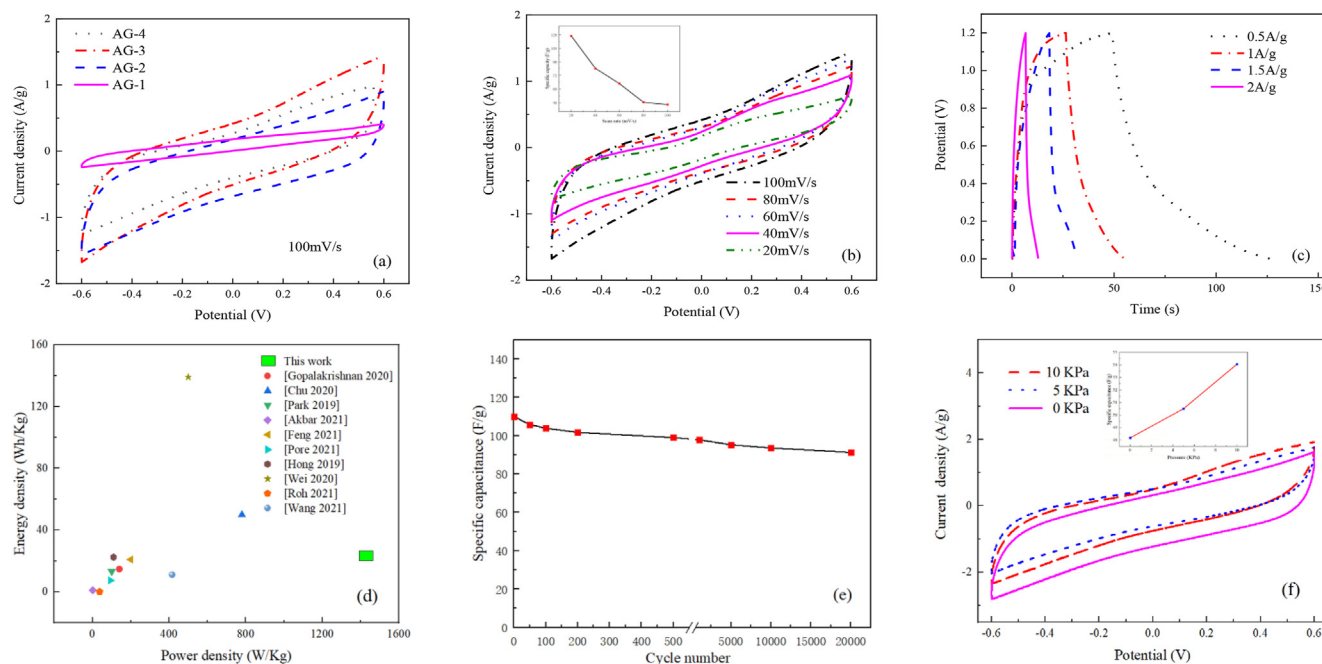
Fig. 8 − I−V curves of (a) the antimonene/graphene composite sponges under different filler ratios and (b) the AG-3 sample under different temperatures.

pure graphene composite sponge electrodes. This implied the suitability of antimonene as a filler in the functional devices used as supercapacitors due to its excellent electrochemical performance. At the high scan rate of 100 mV/s, the specific capacity of the functional device with AG-3 electrodes is significantly higher than others as shown in Fig. 9a. The specific capacitance values of the functional devices with AG-1, AG-2, AG-3 and AG-4 samples calculated by CV curve were 12.3, 27.0, 43.8, and 28.8 F/g, respectively. As the content of antimonene increased, the specific capacitance value increased to certain extend as the result of the combined action of the increase of electrochemical active charge and the increase of electrochemical bilayer on the material surface. However, the decreased specific capacitance of the AG-4-

loaded device is likely to be due to the presence of aggregates, which reduced their electroactive surface area and the ability to carry electrons and ions. Therefore, we focused on the functional device made with AG-3 samples to further study their other functions or properties because it has the highest specific capacitance value.

As revealed in Fig. 9b, the CV curves show a quasi-parallelogram shape and mirror-image symmetry at scanning rates ranging from 20 to 100 mV/s. When the scanning rate increased from 20 to 100 mV/s, the specific capacitance calculated by CV curve was 119.0, 83.0, 66.0, 45.3, and 42.8 F/g, respectively. The specific capacitance of the functional devices decreased with the increase in scanning rate (Fig. 9b Insert). The linear dependence of current ranges with respect

Fig. 9 − Electrochemical characterization of the functional devices based on antimonene/graphene composite sponges: (a) CV curves of devices with different composites obtained at 100 mV/s, (b) CV curves at various scan rate, inset: comparative specific capacity of AG-3 electrodes as a function of scan rate, (c) GCD curves, (d) ragone plots of the devices compared with previously reported results, (e) cyclic stability of the AG-3 supercapacitor and (f) CV curves of AG-3 devices under different pressures, inset: relationship between specific capacitance and pressure.

to the applied scan rate highlights the ideal capacitive nature of the functional device.

In addition, the linear profile and symmetric triangular-like shape of GCD curves at different current densities ranging from 0.5 to 2.0 A/g and a potential window of −0.6 to 0.6 V are shown in Fig. 9c. A typical reversible charging and discharging process is observed at the interface between the electrolyte and electrodes. The specific capacitance values of the supercapacitor at diverse current densities were calculated as 108.5, 79.3, 58.7 and 41.4 F/g, respectively. The discharge time and the specific capacitance decreased with the increase in current density. The supercapacitor achieved a value of 108.5 F/g at 0.5 A/g, which was higher than other reported graphene sponge electrolyte-based supercapacitors [62,63] (Table S1 in the Supporting Information). Moreover, this device had energy density of 23.8 Wh/kg and power density of 1428 W/kg, which are higher than the works reported previously [64—73] as shown in Fig. 9d. The exceptional electrochemical performance was associated with the relatively high ionic transporting efficiency of few-layer antimonene, the large surfaces area of graphene sheets, as well as the strong bond increase in contact area between the interface of electrolyte and electrode, which would decrease the interfacial energy loss.

Figure 9e shows that the capacitance retention was 83% after 20,000 repeated charging/discharge cycles. Although a slightly reduced capacitance retention was observed, the functional device displayed superior cycling stability. The main factor can be ascribed to the stable network structure and the high mechanical strength, which provided protection for ions transportation. The small reduction in specific capacitance was related to the small expansion and contraction deformation of graphene and antimonene sheets during charging and discharging.

In addition, the capacitance of the device varies with the applied pressure. Figure 9f shows CV curves under different pressures. It can be seen that with the increase of pressure, the curve area gradually increases, indicating the increase of specific capacitance value, that is, the improvement of electrochemical performance. This change of the capacitance along with pressure due to the change of ion migration and other factors is helpful for the pressure detection as a capacitive sensor. It is notable that the capacitance changes linearly with the increase of pressure from 0 to 10 kPa, as shown in the inset of Fig. 9f. As a result, pressure can be read from the specific capacitance variation. Such properties render the device additional advantage for developing wearable devices.

We then applied the functional device as a flexible all-solid-state supercapacitor connected to a closed-circuit equipped with a light-emitting diode (LED) (Fig. 10). Three functional devices were connected in series, while the electrochemical workstation charged them. After disconnecting the charging device, the LED illuminated for 3s. The experiment shows that the functional device has the potential to store energy, while further investigations will be carried out to improve their performance.

3.6. Sensing property of the functional device

Because the functional device has good electrochemical performance, it is further designed to be used as capacitance sensor to monitor pressure. The sensitivity of the capacitive sensor in this work is defined as [29].

$$S = ((C-C_0)/C_0)/P = (\Delta C/C_0)/P \tag{4}$$

where S is the sensitivity, C is the real-time capacitance value, C_0 is the initial capacitance value, and P is the applied pressure.

Based on the excellent electrochemical property of the AG-3-fabricated functional devices, we will explore the influence of the addition of antimonene on their sensing performance compared with that of AG-1 ones. In this work, electrochemical workstations were used to collect electrochemical performance data and different weights were used to represent the applied loads to characterize a series of performance of the functional device used as capacitive sensor.

As presented in Fig. 11a, two regions of approximately linear relationship between sensitivity and applied pressure were observed in the pressure range of 0—24.5 kPa. The relative capacitance change ($\Delta C/C_0$) of the AG-3-fabricated sensor increased firstly with the $S_1 = 0.013$ kPa^{-1} during the intensity of pressure range of 0—9.8 kPa, while slightly raised with the $S_2 = 0.007$ kPa^{-1} for the intensity of pressure range of 9.8—24.5 kPa. AG-3 has good linearity and high sensitivity over a wide pressure range, which is mainly attributed to the following three points: (1) The porous structure of sponge has high compressibility, which ensures a wide pressure range. (2) The organized layered structure of graphene achieves effective stress transfer so that the rate of capacitance changes with pressure stably. (3) As the applied pressure or strain increases, the contact area between these graphene sheets and antimonene sheets increases. As a result, the capacitance of the composite material changes. Thus, this unique structure
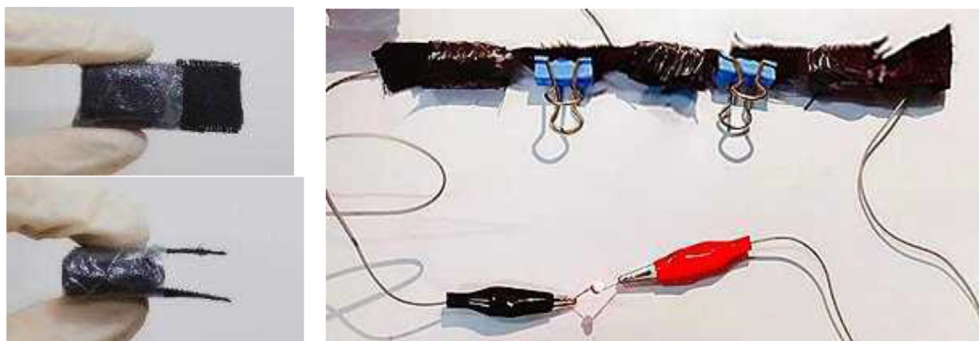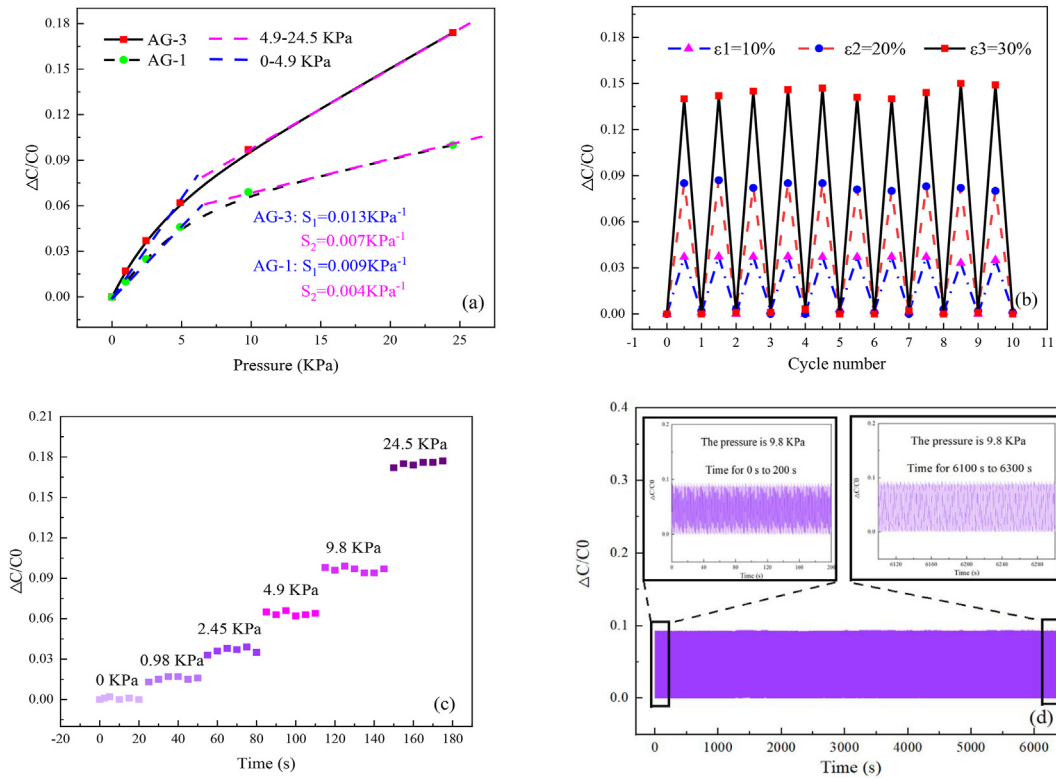

Fig. 10 — Energy storage capacity test.

Fig. 11 — (a) Relative capacitance—pressure response curves of the AG-1 and AG-3 capacitive sensors; (b) capacitance response of repeatedly compressing tests of capacitive sensor at different pressure strains (10, 20, and 30%); (c) pressure-capacitance responses of the relative capacitance change of capacitive sensor from 0 to 24.5 kPa; and (d) capacitance response of capacitive sensor by applying pressure at 9.8 kPa for 20,000 cycles.

results in maintaining linear sensitivity over a wider range of pressures. The sensitivity of the AG-1-fabricated sensor is also divided into two linear regions. However, the sensitivity of the AG-1-fabricated sensor is much lower than that of AG-3-fabricated sensor. Therefore, other sensing performances of the AG-1-fabricated sensor will be tested in the later experiments.

Different strains were applied to the capacitive sensor to assess the repeatability and reliability of sensing capability under a wide strain range. A series of cyclic compressing with a constant strain was carried out to obtain the relative capacitance changes with different strains (Fig. 11b). The response curves presented high linearity and repeatability. Originally, the $\triangle C/C_0$ approached to 0 at a strain of 0%. A fast and distinguishable stability response was then successfully acquired for both the loading and releasing process. The capacitance change rate increased with the increase in the level of strains under the same pressure. The capacitance change rate of the capacitive sensor was stable under the same strain, which indicated that the functional device had stable sensing performance and good reproducibility.

Next, the stair-type pressures were applied to the sensor (Fig. 11c). It was obviously displayed that $\triangle C/C_0$ increased in a similar pattern as step-wise compressing-holding process, while $\triangle C/C_0$ remained almost unchanged at the same pressure. This result indicated the excellent signal stability. Particularly, it demonstrated that the sensor prepared in this work can distinguish pressures as low as 0.98 kPa.

In order to verify and simulate the stable performance of the capacitive sensor in real life, 20,000-cycle fatigue test was carried out. The capacitance changes of the developed sensor were continuously recorded at 9.8 kPa, when more than 20,000 cycles of loading/unloading pressure were repeatedly applied (Fig. 11d). During long-term durability test process, the capacitance variation was tracked in ambient conditions with sealing. It is evident that the baseline capacitance did not drift under repeated load-unload pressures, further demonstrating the robustness of capacitive sensor to various compression stimuli. The capacitive sensor exhibited high durability and repeatability. Comparing with the initial and last 200 s (Fig. 11d inset), the relative capacitance changes of the capacitive sensor had no noticeable deterioration, while only small hysteresis variations were observed. The high cyclic stability is due to the fact that the elastic structure of the sponge is almost not damaged by the pressure applied during the test, while the modified antimonene sheets and graphene sheets have good electrochemical stability and good adhesion on sponge skeleton in accordance with SEM images in Fig. S10 in the Supporting Information.

We had demonstrated that applied pressure to the capacitive sensor caused a significant change in the electrochemical signals. The working principle of capacitive sensor was illustrated in Fig. S9 of the Supporting Information. Graphene and antimonene that absorbed on the sponge skeleton provided more removable charges. Owing to the existence of graphene, antimonene and the elastic structure of sponge, the pressure

strain caused the change of capacitance value of capacitance sensor, which endowed the functional device with pressure sensitivity ability. Based on the overall performance and unique characteristics, this capacitive sensor showed great potential to be used as wearable integrated sensory system.

3.7. Powered flexible sensing system

Although many supercapacitors and graphene-based capacitive sensors have been developed, their application in integrated electronic devices is still challenging. In order to achieve the integration goal, the functional devices were connected with both the capacitive sensor and supercapacitors in series to form a complete circuit, as shown in Figure 12a and b. After charging supercapacitors with an electrochemical workstation

at a turn-on voltage, the connected flexible capacitive sensor was working supported by the charging supercapacitors.

The current changes of the functional devices under the pressure of 3.27 kPa for 7 cycles was monitored over 40 s (Fig. 12c). The changes of the original electronic signal were because of the energy consumption during self-discharging process. When mechanical pressure was applied, the sensor was compressed, resulting in the dramatic increase of current. In contrast, during the holding state, the current of sensor remained stable. The responding curve showed that this sensing system exhibited excellent sensitivity and stability. Upon cyclic compressing and releasing at a constant pressure of 1.63 kPa, the current signal of the sensor showed similar patterns, while the relative signal drift of the capacitive sensor was acceptable during the 1500 cyclic loading (Fig. 12d). This
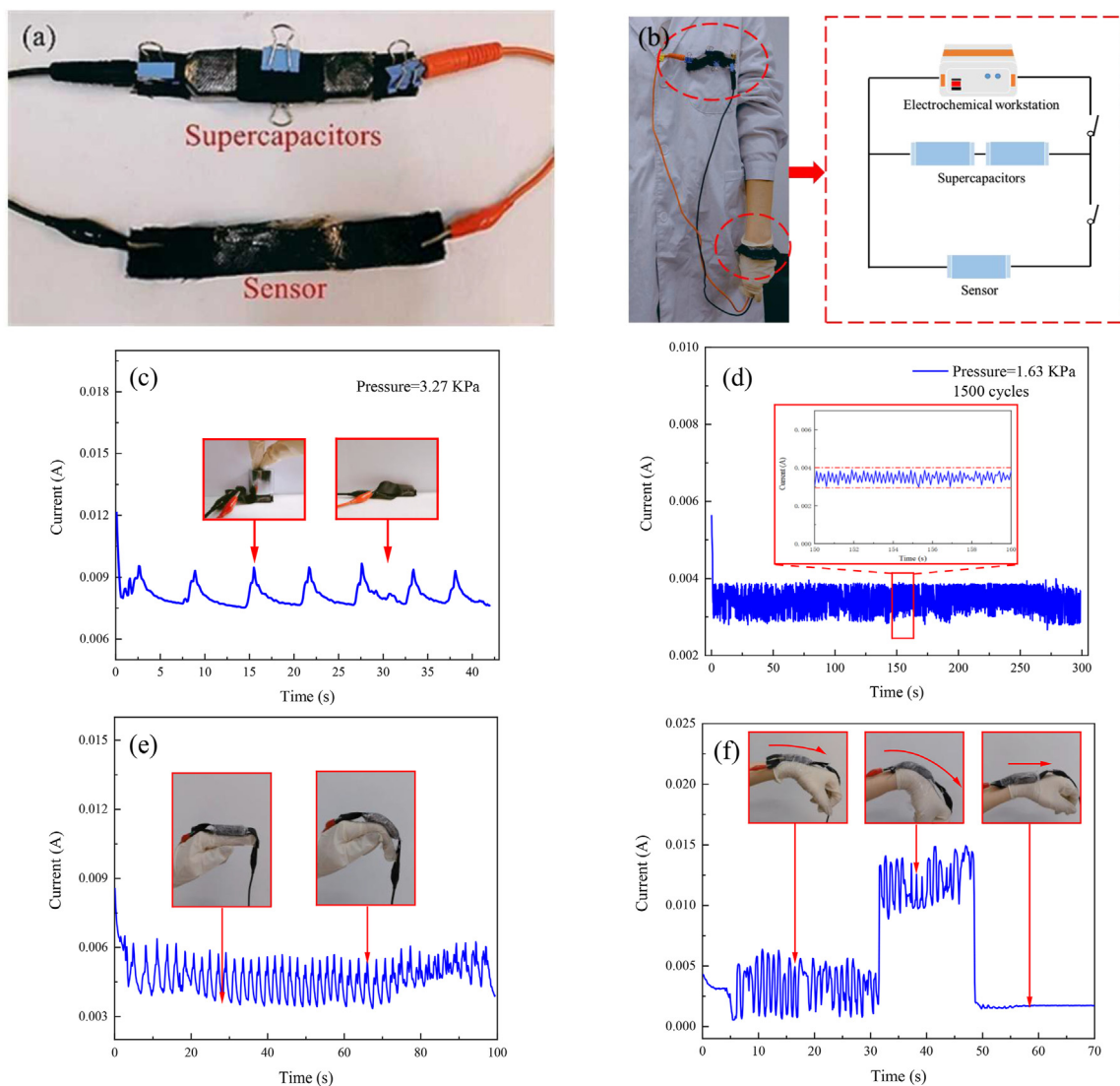
Fig. 12 – Electrical signal responsiveness of the functional devices: (a) the diagram of the powered flexible sensing system; (b)photograph of the flexible sensing system consist of the supercapacitor placed onto the coat surfaces and sensors attached to the skin, and the schematics of the complete circuit; (c) current response curve of the sensor upon compressing and relaxing under pressure of 3.27 kPa for 7 cycles; and (d) the current response curve under pressure of 1.63 kPa for 1500 cycles, while the inset showed the relative current change from 150 s to 160 s, current response curves of the sensing system as the human motion monitoring with (e) finger movement and (f) wrist movement.

allows the reliable practical utilization of the developed powered sensing system.

The flexible sensor system was mounted on the finger and wrist to monitor human motion processes. During cyclic finger bending at a certain angel, the sensor exhibited a stable current response (Fig. 12e). Similarly, the sensor detected the current changes in response to different motion with an increase in angles (Fig. 12f). The attached sensor was compressed when the bending angle increased, resulting in increased maximum value in current change. The results indicated that the powered flexible sensing system has great potential to be used for monitoring human motion signals.

4. Summary and conclusions

In summary, we have developed a multifunctional and durable graphene-based composite sponge doped with antimonene nanosheets as flexible supercapacitor and sensitive pressure sensor. Based on melamine sponge with regular pore structure, the best content combination of antimonene and graphene have been systematically investigated to improve the structural regularity, electrochemical property and sensitivity of device. By preparing the antimonene/graphene composite sponge with a mass ratio of graphene to antimony of 1:1.5, the flexible supercapacitor was obtained with the specific capacitance of 119.0 F/g. The obtained pressure sensor showed excellent sensitivity, low detection limit, high flexibility, and high mechanical, temperature and sensing stability. Owing to its good multifunctional performances, the proposed pressure sensor has been successfully applied as supercapacitors and human motion monitors to detect human movement signals such as finger and wrist deformation. This research has demonstrated the potentials of the antimonene/graphene composite sponge to fabricate flexible electronic devices in the fields of biomedicine and electrochemistry.

Declaration of Competing Interest

The authors declare that they have no known competing financial interests or personal relationships that could have appeared to influence the work reported in this paper.

Acknowledgment

Appendix A. Supplementary data

Supplementary data to this article can be found online at https://doi.org/10.1016/j.jmrt.2022.02.009.

REFERENCES

[1] Lv H, Li Y, Jia Z, Wang L, Guo X, Zhao B, et al. Exceptionally porous three-dimensional architectural nanostructure derived from CNTs/graphene aerogel towards the ultra-wideband EM absorption. Compos B Eng 2020:196.

[2] Zhang F, Cui W, Wang B, Xu B, Liu X, Liu X, et al. Morphology-control synthesis of polyaniline decorative porous carbon with remarkable electromagnetic wave absorption capabilities. Compos B Eng 2021:204.

[3] Feng C, Yi Z, Jin X, Seraji SM, Dong Y, Kong L, et al. Solvent crystallization-induced porous polyurethane/graphene composite foams for pressure sensing. Compos B Eng 2020:194.

[4] Lou J, Liu Y, Wang Z, Zhao D, Song C, Wu J, et al. Bioinspired multifunctional paper-based rGO composites for solar-driven clean water generation. ACS Appl Mater Interfaces 2016;8:14628–36.

[5] Liu J, Zhang L, Yang C, Tao S. Preparation of multifunctional porous carbon electrodes through direct laser writing on a phenolic resin film. J Mater Chem 2019;7:21168–75.

[6] Narayana KJ, Gupta Burela R. A review of recent research on multifunctional composite materials and structures with their applications. Mater Today Proc 2018;5:5580–90.

[7] Hong Y, Li C, Yin B, Li D, Zhang Z, Mao B, et al. Promoting visible-light-induced photocatalytic degradation of tetracycline by an efficient and stable beta-Bi2O3@g-C3N4 core/shell nanocomposite. Chem Eng J 2018;338:137–46.

[8] Dai J, Tian Q, Sun Q, Wei W, Zhuang J, Liu M, et al. TiO2-alginate composite aerogels as novel oil/water separation and wastewater remediation filters. Compos B Eng 2019;160:480–7.

[9] Zhao X, Yang F, Wang Z, Ma P, Dong W, Hou H, et al. Mechanically strong and thermally insulating polyimide aerogels by homogeneity reinforcement of electrospun nanofibers. Compos B Eng 2020:182.

[10] Li J, Ding Y, Gao Q, Zhang H, He X, Ma Z, et al. Ultrathin and flexible biomass-derived C@CoFe nanocomposite films for efficient electromagnetic interference shielding. Compos B Eng 2020:190.

[11] Ren C, Ding X, Li W, Wu H, Yang H. Highly efficient adsorption of heavy metals onto novel magnetic porous composites modified with amino groups. J Chem Eng Data 2017;62:1865–75.

[12] Li G, Li Y, Chen J, Zhao P, Li D, Dong Y, et al. Synthesis and research of egg shell-yolk NiO/C porous composites as lithium-ion battery anode material. Electrochim Acta 2017;245:941–8.

[13] Silva MA, Rocha CV, Gallo J, Felgueiras HP, de Amorim MTP. Porous composites based on cellulose acetate and alfa-hematite with optical and antimicrobial properties. Carbohydr Polym 2020;241:116362.

[14] Cheng Y, Zhao Y, Zhao H, Lv H, Qi X, Cao J, et al. Engineering morphology configurations of hierarchical flower-like MoSe2 spheres enable excellent low-frequency and selective microwave response properties. Chem Eng J 2019;372:390–8.

[15] Lu X, Zheng Y, Yang J, Qu J. Multifunctional paraffin wax/carbon nanotube sponge composites with simultaneous

high-efficient thermal management and electromagnetic interference shielding efficiencies for electronic devices. Compos B Eng 2020:199.

[16] Jia Y, Yue X, Wang Y, Yan C, Zheng G, Dai K, et al. Multifunctional stretchable strain sensor based on polydopamine/reduced graphene oxide/electrospun thermoplastic polyurethane fibrous mats for human motion detection and environment monitoring. Compos B Eng 2020:183.

[17] Li Y, Liu J, Wang S, Zhang L, Shen B. Self-templating graphene network composites by flame carbonization for excellent electromagnetic interference shielding. Compos B Eng 2020:182.

[18] Ding Y, Zhu J, Wang C, Dai B, Li Y, Qin Y, et al. Multifunctional three-dimensional graphene nanoribbons composite sponge. Carbon 2016;104:133—40.

[19] Ha Y, Shi L, Yan X, Chen Z, Li Y, Xu W, et al. Multifunctional electrocatalysis on a porous N-doped NiCo2O4@C nanonetwork. ACS Appl Mater Interfaces 2019;11:45546—53.

[20] Sun B, McCay RN, Goswami S, Xu Y, Zhang C, Ling Y, et al. Gas-permeable, multifunctional on-skin electronics based on laser-induced porous graphene and sugar-templated elastomer sponges. Adv Mater 2018;30:e1804327.

[21] Zhang Y, Wang N, Sun C, Lu Z, Xue P, Tang B, et al. 3D spongy CoS2 nanoparticles/carbon composite as high-performance anode material for lithium/sodium ion batteries. Chem Eng J 2018;332:370—6.

[22] Tahernejad-Javazmi F, Shabani-Nooshabadi M, Karimi-Maleh H. 3D reduced graphene oxide/FeNi3-ionic liquid nanocomposite modified sensor; an electrical synergic effect for development of tert-butylhydroquinone and folic acid sensor. Compos B Eng 2019;172:666—70.

[23] Badakhsh A, Lee Y-M, Rhee KY, Park CW, An K-H, Kim B-J. Improvement of thermal, electrical and mechanical properties of composites using a synergistic network of length controlled-CNTs and graphene nanoplatelets. Compos B Eng 2019:175.

[24] Papageorgiou DG, Kinloch IA, Young RJ. Mechanical properties of graphene and graphene-based nanocomposites. Prog Mater Sci 2017;90:75—127.

[25] Zan YN, Zhang Q, Zhou YT, Liu ZY, Wang QZ, Wang D, et al. Introducing graphene (reduced graphene oxide) into Al matrix composites for enhanced high-temperature strength. Compos B Eng 2020:195.

[26] Chen Y, Hou X, Liao M, Dai W, Wang Z, Yan C, et al. Constructing a "pea-pod-like" alumina-graphene binary architecture for enhancing thermal conductivity of epoxy composite. Chem Eng J 2020:381.

[27] Rafiee M, Nitzsche F, Laliberte J, Hind S, Robitaille F, Labrosse MR. Thermal properties of doubly reinforced fiberglass/epoxy composites with graphene nanoplatelets, graphene oxide and reduced-graphene oxide. Compos B Eng 2019;164:1—9.

[28] Tiwari SK, Sahoo S, Wang N, Huczko A. Graphene research and their outputs: status and prospect. J Sci: Advanced Materials and Devices 2020;5:10—29.

[29] Chen C, Xi J, Han Y, Peng L, Gao W, Xu Z, et al. Ultralight graphene micro-popcorns for multifunctional composite applications. Carbon 2018;139:545—55.

[30] Qiu S, Liu G, Li W, Zhao H, Wang L. Noncovalent exfoliation of graphene and its multifunctional composite coating with enhanced anticorrosion and tribological performance. J Alloys Compd 2018;747:60—70.

[31] Gablech I, Pekárek J, Klempa J, Svatoš V, Sajedi-Moghaddam A, Neužil P, et al. Monoelemental 2D materials-based field effect transistors for sensing and biosensing: phosphorene, antimonene, arsenene, silicene, and germanene go beyond graphene. Trac Trends Anal Chem 2018;105:251—62.

[32] Ares P, Palacios JJ, Abellan G, Gomez-Herrero J, Zamora F. Recent progress on antimonene: a new bidimensional material. Adv Mater 2018;30.

[33] Ji J, Song X, Liu J, Yan Z, Huo C, Zhang S, et al. Two-dimensional antimonene single crystals grown by van der Waals epitaxy. Nat Commun 2016;7:13352.

[34] Wang X, Song J, Qu J. Antimonene: from experimental preparation to practical application. Angew Chem Int Ed Engl 2019;58:1574—84.

[35] Lei T, Li J-M, Li F-S, Wang J-O, Ibrahim K, Zhang K. Anisotropic electronic structure of antimonene. Appl Phys Lett 2019;115.

[36] Wang X, Yu X, Song J, Huang W, Xiang Y, Dai X, et al. Two-dimensional semiconducting antimonene in nanophotonic applications — a review. Chem Eng J 2021:406.

[37] Shao Y, Liu ZL, Cheng C, Wu X, Liu H, Liu C, et al. Epitaxial growth of flat antimonene monolayer: a new honeycomb analogue of graphene. Nano Lett 2018;18:2133—9.

[38] Chen X, Yang Q, Meng R, Jiang J, Liang Q, Tan C, et al. The electronic and optical properties of novel germanene and antimonene heterostructures. J Mater Chem C 2016;4:5434—41.

[39] Tao W, Ji X, Zhu X, Li L, Wang J, Zhang Y, et al. Two-dimensional antimonene-based photonic nanomedicine for cancer theranostics. Adv Mater 2018;30:e1802061.

[40] Lu L, Tang X, Cao R, Wu L, Li Z, Jing G, et al. Broadband nonlinear optical response in few-layer antimonene and antimonene quantum dots: a promising optical kerr media with enhanced stability. Adv Opt Mater 2017;5.

[41] Xiao Q, Hu C-X, Wu H-R, Ren Y-Y, Li X-Y, Yang Q-Q, et al. Antimonene-based flexible photodetector. Nanoscale Horizons 2020;5:124—30.

[42] Zhang F, Wang M, Wang Z, Han K, Liu X, Xu X. Excellent nonlinear absorption properties of β-antimonene nanosheets. J Mater Chem C 2018;6:2848—53.

[43] Gibaja C, Rodriguez-San-Miguel D, Ares P, Gomez-Herrero J, Varela M, Gillen R, et al. Few-layer antimonene by liquid-phase exfoliation. Angew Chem Int Ed Engl 2016;55:14345—9.

[44] Mao Y-H, Zhang L-F, Wang H-L, Shan H, Zhai X-F, Hu Z-P, et al. Epitaxial growth of highly strained antimonene on Ag(111). Frontiers of Physics 2018;13.

[45] Fortin-Deschenes M, Waller O, Mentes TO, Locatelli A, Mukherjee S, Genuzio F, et al. Synthesis of antimonene on germanium. Nano Lett 2017;17:4970—5.

[46] Singal S, Joshi A, Singh G, Sharma RK. Dual approach of antimonene hybridization and hierarchical structuration to expose more active sites for improved charge storage characteristics of VS4. J Power Sources 2020:475.

[47] Tian W, Zhang S, Huo C, Zhu D, Li Q, Wang L, et al. Few-layer antimonene: anisotropic expansion and reversible crystalline-phase evolution enable large-capacity and long-life Na-ion batteries. ACS Nano 2018;12:1887—93.

[48] Sengupta A, Frauenheim T. Lithium and sodium adsorption properties of monolayer antimonene. Mater Today Energy 2017;5:347—54.

[49] Martínez-Periñán E, Down MP, Gibaja C, Lorenzo E, Zamora F, Banks CE. Antimonene: a novel 2D nanomaterial for supercapacitor applications. Adv Energy Mater 2018;8.

[50] Song Y, Liang Z, Jiang X, Chen Y, Li Z, Lu L, et al. Few-layer antimonene decorated microfiber: ultra-short pulse generation and all-optical thresholding with enhanced long term stability. 2D Mater 2017;4.

[51] Su J, Li W, Duan T, Xiao B, Wang X, Pei Y, et al. Graphene/antimonene/graphene heterostructure: a potential anode for sodium-ion batteries. Carbon 2019;153:767—75.

[52] Wang X, Tang C, Zhou X, Zhu W, Cheng C. Theoretical investigating of graphene/antimonene heterostructure as a

promising high cycle capability anodes for fast-charging lithium ion batteries. Appl Surf Sci 2019;491:451—9.

[53] Wu P, Li P, Huang M. Potential application of graphene/antimonene herterostructure as an anode for Li-ion batteries: a first-principles study. Nanomaterials 2019;9.

[54] Cui X, Tian J, Yu Y, Chand A, Zhang S, Meng Q, et al. Multifunctional graphene-based composite sponge. Sensors 2020:20.

[55] Meng Q, Yu Y, Tian J, Yang Z, Guo S, Cai R, et al. Multifunctional, durable and highly conductive graphene/sponge nanocomposites. Nanotechnology 2020;31:465502.

[56] Yang H, Kannappan S, Pandian AS, Jang JH, Lee YS, Lu W. Graphene supercapacitor with both high power and energy density. Nanotechnology 2017;28:445401.

[57] Yi F-L, Meng F-C, Li Y-Q, Huang P, Hu N, Liao K, et al. Highly stretchable CNT Fiber/PAAm hydrogel composite simultaneously serving as strain sensor and supercapacitor. Compos B Eng 2020:198.

[58] Song Y, Ran A, Peng Z, Huang W, Huang B, Jian X, et al. Cobalt Diselenide@Reduced graphene oxide based nanohybrid for supercapacitor applications. Compos B Eng 2019:174.

[59] Song Y, Chen H, Su Z, Chen X, Miao L, Zhang J, et al. Highly compressible integrated supercapacitor-piezoresistance-sensor system with CNT-PDMS sponge for Health monitoring. Small 2017;13.

[60] Zhang S-W, Yin B-S, Liu C, Wang Z-B, Gu D-M. A lightweight, compressible and portable sponge-based supercapacitor for future power supply. Chem Eng J 2018;349:509—21.

[61] Lee J, Kim J, Shin Y, Jung I. Ultra-robust wide-range pressure sensor with fast response based on polyurethane foam doubly coated with conformal silicone rubber and CNT/TPU nanocomposites islands. Compos B Eng 2019:177.

[62] Huang J, Peng S, Gu J, Chen G, Gao J, Zhang J, et al. Self-powered integrated system of a strain sensor and flexible all-solid-state supercapacitor by using a high performance ionic organohydrogel. Materials Horizons 2020;7:2085—96.

[63] Kshetri T, Tran DT, Singh TI, Kim NH, Lau K-t, Lee JH. Effects of the composition of reduced graphene oxide/carbon nanofiber nanocomposite on charge storage behaviors. Compos B Eng 2019:178.

[64] Gopalakrishnan A, Yu A, Badhulika S. Three-dimensional nitrogen rich bubbled porous carbon sponge for supercapacitor & pressure sensing applications. Int J Energy Res 2020;44:7242—53.

[65] Chu D, Li F, Song X, Ma H, Tan L, Pang H, et al. A novel dual-tasking hollow cube NiFe2O4-NiCo-LDH@rGO hierarchical material for high performance supercapacitor and glucose sensor. J Colloid Interface Sci 2020;568:130—8.

[66] Park H, Kim JW, Hong SY, Lee G, Lee H, Song C, et al. Dynamically stretchable supercapacitor for powering an integrated biosensor in an all-in-one textile system. ACS Nano 2019;13:10469—80.

[67] Akbar Sial Q, Thai Duy L, Singh R, Iqbal S, Yeasmin R, Lee Y-J, et al. A multifunctional TiN/Ni electrode for wearable supercapacitor and sensor with an insight into charge storage mechanism. Appl Surf Sci 2021:555.

[68] Feng E, Li J, Zheng G, Yan Z, Li X, Gao W, et al. Long-term anti-freezing active organohydrogel based superior flexible supercapacitor and strain sensor. ACS Sustainable Chem Eng 2021;9:7267—76.

[69] Pore OC, Fulari AV, Kamble RK, Shelake AS, Velhal NB, Fulari VJ, et al. Hydrothermally synthesized Co3O4 microflakes for supercapacitor and non-enzymatic glucose sensor. J Mater Sci Mater Electron 2021;32:20742—54.

[70] Hong S, Yuan Y, Liu C, Chen W, Chen L, Lian H, et al. A stretchable and compressible ion gel based on a deep eutectic solvent applied as a strain sensor and electrolyte for supercapacitors. J Mater Chem C 2020;8:550—60.

[71] Wei N, Wu J, Tang Y, Lu S, Wang L. Self-powered supercapacitor-mode tactile sensor based on polygonal litchi—like nanospheres decorated three-dimensional reduced graphene oxide aerogel for wearable electronics device. J Power Sources 2020:479.

[72] Roh HD, Deka BK, Park HW, Park Y-B. Multifunctional composite as a structural supercapacitor and self-sensing sensor using NiCo2O4 nanowires and ionic liquid. Compos Sci Technol 2021:213.

[73] Wang X, Zhang D, Zhang H, Gong L, Yang Y, Zhao W, et al. In situ polymerized polyaniline/MXene (V2C) as building blocks of supercapacitor and ammonia sensor self-powered by electromagnetic-triboelectric hybrid generator. Nano Energy 2021:88.